Aalto University

OPEN ACCESS

This is an electronic reprint of the original article.
This reprint may differ from the original in pagination and typographic detail.

Nieminen, Jaakko O.; Stenroos, Matti

The magnetic field inside a layered anisotropic spherical conductor due to internal sources

Published in:
Journal of Applied Physics

DOI:
10.1063/1.4939469

Published: 14/01/2016

Document Version
Publisher's PDF, also known as Version of record

Please cite the original version:
Nieminen, J. O., & Stenroos, M. (2016). The magnetic field inside a layered anisotropic spherical conductor due to internal sources. *Journal of Applied Physics*, *119*(2), 1-12. Article 023901. https://doi.org/10.1063/1.4939469

This material is protected by copyright and other intellectual property rights, and duplication or sale of all or part of any of the repository collections is not permitted, except that material may be duplicated by you for your research use or educational purposes in electronic or print form. You must obtain permission for any other use. Electronic or print copies may not be offered, whether for sale or otherwise to anyone who is not an authorised user.

The magnetic field inside a layered anisotropic spherical conductor due to internal sources

Jaakko O. Nieminen, and Matti Stenroos

Citation: Journal of Applied Physics **119**, 023901 (2016); doi: 10.1063/1.4939469
View online: https://doi.org/10.1063/1.4939469
View Table of Contents: http://aip.scitation.org/toc/jap/119/2
Published by the American Institute of Physics

Articles you may be interested in

Acoustic scattering from inhomogeneous spheres with impenetrable cores
Journal of Applied Physics **119**, 014902 (2016); 10.1063/1.4939292

JOURNAL OF APPLIED PHYSICS **119**, 023901 (2016)

The magnetic field inside a layered anisotropic spherical conductor due to internal sources

Jaakko O. Nieminen[1,2,a] and Matti Stenroos[1]
[1]*Department of Neuroscience and Biomedical Engineering, Aalto University School of Science, P.O. Box 12200, FI-00076 AALTO, Finland*
[2]*Department of Psychiatry, University of Wisconsin–Madison, 6001 Research Park Blvd., Madison, Wisconsin 53719, USA*

(Received 25 November 2015; accepted 21 December 2015; published online 8 January 2016)

Recent advances in neuronal current imaging using magnetic resonance imaging and in invasive measurement of neuronal magnetic fields have given a need for methods to compute the magnetic field inside a volume conductor due to source currents that are within the conductor. In this work, we derive, verify, and demonstrate an analytical expression for the magnetic field inside an anisotropic multilayer spherically symmetric conductor due to an internal current dipole. We casted an existing solution for electric field to vector spherical harmonic (VSH) form. Next, we wrote an ansatz for the magnetic field using toroidal–poloidal decomposition that uses the same VSHs. Using properties of toroidal and poloidal components and VSHs and applying magnetic scalar potential, we then formulated a series expression for the magnetic field. The convergence of the solution was accelerated by formulating the solution using an addition–subtraction method. We verified the resulting formula against boundary-element method. The verification showed that the formulas and implementation are correct; 99th percentiles of amplitude and angle differences between the solutions were below 0.5% and 0.5°, respectively. As expected, the addition–subtraction model converged faster than the unaccelerated model; close to the source, 250 terms gave relative error below 1%, and the number of needed terms drops fast, as the distance to the source increases. Depending on model conductivities and source position, field patterns inside a layered sphere may differ considerably from those in a homogeneous sphere. In addition to being a practical modeling tool, the derived solution can be used to verify numerical methods, especially finite-element method, inside layered anisotropic conductors. © *2016 AIP Publishing LLC*.
[http://dx.doi.org/10.1063/1.4939469]

I. INTRODUCTION

There is an increasing interest in characterizing neuronal activity via measuring magnetic field generated by neurons. In addition to well-established magnetoencephalography (MEG)[1] that is based on measuring the neuromagnetic field outside the head, novel approaches that measure magnetic field inside the head are receiving attention. Direct neural imaging (DNI), also termed as neuronal current imaging, aims to detect neuronal activity directly in high[2–4] or ultra-low magnetic field.[5–7] The basic idea in these is to measure changes in the magnetic resonance signal due to altered spin dynamics caused by the magnetic field arising from the neuronal activity. In smaller scale, technology for invasive measurement of neuromagnetic fields inside the head, even directly in the cortex, is being developed. These modalities are based on diamond sensors[8–10] or spintronics.[11]

To better understand the feasibility of these new modalities and to optimize imaging approaches and sensor designs, a measurement model that links neuronal sources to measured signals is needed. A key part of such a model is a volume conductor model that characterizes the effect of head conductivity profile on neurally driven electric currents and magnetic fields. Volume conductor models used in electroencephalography (EEG) typically contain three (or four) layered compartments of homogeneous conductivity: the brain, (cerebrospinal fluid (CSF)), skull, and scalp, while MEG modeling has been mainly carried out with single-shell (inner skull) or three-shell models.[12] Extending from the four-compartment model, the brain can be further separated into gray and white matter, and the anisotropy of the white matter can be taken into account.[13]

In experimental MEG work, a spherically symmetric head model has been widely used as a simplified description of conductivity. Magnetic field outside the head is independent of radial conductivity profile in spherical geometry, allowing simple closed-form implementation of the model.[14] Furthermore, an arbitrary asymmetric distribution of radial anisotropy, i.e., difference between the radial and tangential conductivity, in an otherwise spherically symmetric conductor has no effect on the external magnetic field due to internal sources.[15] Inside the head, the modelling is more complicated: as will be shown in this work, the radial conductivity profile and anisotropy influence the internal magnetic field.

So far, analytical formulas for magnetic field inside a spherical conductor have been presented for a homogeneous isotropic model only.[16,17] Solutions for electric potential and

[a]Electronic mail: jaakko.nieminen@aalto.fi

 © 2016 AIP Publishing LLC

electric field in layered and anisotropic spherically symmetric models have previously been presented in Refs. 18–22, but to our knowledge, corresponding formulas for magnetic field have not been presented. In this paper, we derive an analytical expression for the magnetic field inside an anisotropic multilayer spherically symmetric conductor due to an internal current dipole.

In volume conductor modeling, analytical solutions of simplified geometries have played four important roles: First, they provide conceptual understanding of phenomena that leads to useful rules-of-thumb such as "compared with tangential sources, radial sources produce very weak MEG signals."[1] Second, they are used for system calibration and sensor development in connection with physical phantom measurements.[7,23,24] Third, they can be used as practical tools in signal analysis for sources in those regions of the head that show local spherical symmetry.[25] Fourth, they are used for developing and verifying numerical methods that enable more realistic model geometries.[26–28] This work has potential applications in all these areas.

II. METHODS

A. Theory

According to the quasi-static approximation[29] of Maxwell's equations, current density $\boldsymbol{J}$ and the divergence-free magnetic field $\boldsymbol{B}$ are related by

$$\nabla \times \boldsymbol{B} = \mu_0 \boldsymbol{J} = \mu_0 (\boldsymbol{J}_\mathrm{P} + \boldsymbol{J}_\mathrm{V}), \tag{1}$$

where μ_0 is the permeability of vacuum, $\boldsymbol{J}_\mathrm{P}$ denotes the primary current density that gives rise to a charge density and an electric field $\boldsymbol{E}$, $\boldsymbol{J}_\mathrm{V} = \boldsymbol{\sigma}\boldsymbol{E}$ is the volume current density driven by the electric field, and $\boldsymbol{\sigma}$ is the conductivity tensor. In this study, we assume that the off-diagonal elements of the conductivity tensor are zero, i.e., the conductivity is completely described by the diagonal, $\boldsymbol{\sigma}$, of an uniaxial conductivity tensor. In this case, $\boldsymbol{J}_\mathrm{V} = \boldsymbol{\sigma} \circ \boldsymbol{E}$, where the operator "$\circ$" indicates the Hadamard product of two vectors, i.e., their element-wise multiplication (in spherical coordinates, $\boldsymbol{J}_\mathrm{V} = \sigma_r E_r \boldsymbol{e}_r + \sigma_\theta E_\theta \boldsymbol{e}_\theta + \sigma_\phi E_\phi \boldsymbol{e}_\phi$). The primary and volume currents reflect two different generation mechanisms of biomagnetic fields: the primary component due to the neuronal activity and the secondary component due to the ohmic currents driven by the electric field. For simplicity, we have assumed that the permeability of the medium is μ_0, i.e., that of vacuum, which is a good approximation for the human head. Furthermore, under quasi-static approximation, the electric field satisfies $\nabla \times \boldsymbol{E} = 0$ and is thus given by the electric scalar potential V: $\boldsymbol{E} = -\nabla V$. The electric potential and the normal component of $\boldsymbol{J}$ are continuous across conductivity boundaries.[30]

1. Problem geometry and electric field

Let us consider a multilayer spherically symmetric conductor in free space. Let r_k $(0 < r_1 < \ldots < r_K)$ denote the radius of the kth boundary surface and K be the total number of the surfaces. The conductivity in the region between surfaces $k-1$ and k is anisotropic and given by $\boldsymbol{\sigma}_k = [\sigma_{\mathrm{r},k}, \sigma_{\mathrm{t},k}, \sigma_{\mathrm{t},k}]$, where $\sigma_{\mathrm{r},k}$ and $\sigma_{\mathrm{t},k}$ are the radial and tangential conductivities in spherical geometry, respectively. We further assume that $\sigma_{\mathrm{r},k}$ and $\sigma_{\mathrm{t},k}$ are constant within each compartment. Figure 1 illustrates the notation.

The electric potential V inside the sphere due to an internal current dipole $\boldsymbol{J}_\mathrm{P}(\boldsymbol{r}) = \boldsymbol{Q}\delta(\boldsymbol{r} - \boldsymbol{r}_\mathrm{Q})$, where $\boldsymbol{Q}$ is its moment and $\boldsymbol{r}_\mathrm{Q} = [r_\mathrm{Q}, \theta_\mathrm{Q}, \phi_\mathrm{Q}]$ its position in spherical coordinates, is derived in Ref. 19; Reference 22 extends the solution to allow also the innermost layer to be anisotropic. In Appendix B, we write V in our notation using real spherical harmonics Y and real vector spherical harmonics $\boldsymbol{Y}$.

Given the potential, the electric field inside the conductor can be calculated straigthforwardly as $\boldsymbol{E} = -\nabla V$. The result of Ref. 22 can be written compactly using real vector spherical harmonics (Eqs. (A3) and (A5)):

$$\boldsymbol{E}(\boldsymbol{r}) = -\sum_{n=1}^{\infty}\sum_{m=-n}^{n} Q_n^m(\boldsymbol{r}_\mathrm{Q}) \left\{ c_{\xi,k,n}(r) \times \left[\frac{v_{k,n}}{n}, 1, 1\right] \circ \boldsymbol{Y}_{n,n-1}^m(\theta,\phi) + d_{\xi,k,n}(r) \left[\frac{v_{k,n}+1}{n+1}, 1, 1\right] \circ \boldsymbol{Y}_{n,n+1}^m(\theta,\phi) \right\}, \tag{2}$$

where

$$c_{\xi,k,n}(r) = \sqrt{n(2n+1)}\, r^{v_{k,n}-1} a_{\xi,k,n}, \quad r_{k-1} < r < r_k \tag{3}$$

and

$$d_{\xi,k,n}(r) = \sqrt{(n+1)(2n+1)}\, r^{-(v_{k,n}+2)} b_{\xi,k,n}, \quad r_{k-1} < r < r_k. \tag{4}$$

The definitions of Q_n^m, $v_{k,n}$, $a_{\xi,k,n}$, and $b_{\xi,k,n}$ are given in Appendix B. Although not immediately obvious from the form of Eq. (2), the central region of the sphere contains

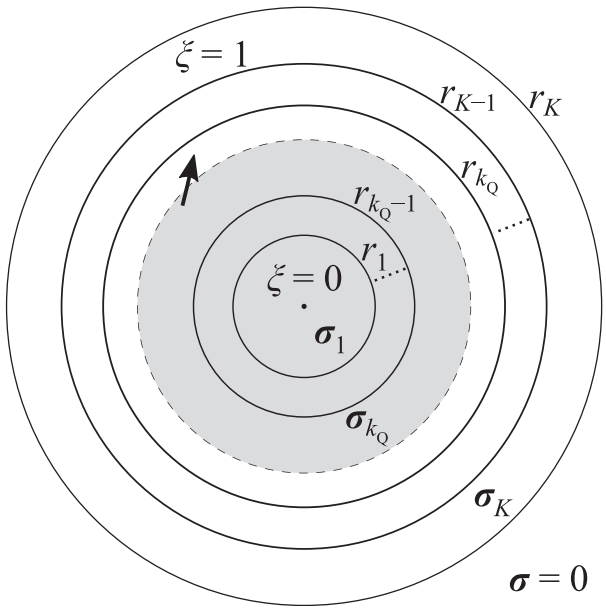

FIG. 1. An illustration of the notation used in the text. The radius of the kth surface is r_k and the conductivity in the region between surfaces $k-1$ and k is $\boldsymbol{\sigma}_k$. The subscript k_Q refers to the layer containing the current dipole. The position and orientation of the dipole are indicated by an arrow. When $r < r_\mathrm{Q}$, $\xi = 0$ (gray area); when $r > r_\mathrm{Q}$, $\xi = 1$ (white area). r_Q is the radial coordinate of the dipole position.

only terms that are regular at the origin; similarly, the terms in the region $r > r_Q$ decay as $r \to \infty$. The associated volume current density in the kth layer is obtained simply as $\boldsymbol{J}_V(\boldsymbol{r}) = [\sigma_{r,k}, \sigma_{t,k}, \sigma_{t,k}] \circ \boldsymbol{E}(\boldsymbol{r})$, $r_{k-1} < r < r_k$.

2. Magnetic field

Because $\nabla \cdot \boldsymbol{B} = 0$, we can express $\boldsymbol{B}$ using the toroidal–poloidal decomposition (a decomposition of divergence-free vector fields used in study of, e.g., plasma physics and geomagnetism; see Appendix A and Ref. 31):

$$\boldsymbol{B}(\boldsymbol{r}) = \underbrace{\sum_{n=1}^{\infty}\sum_{m=-n}^{n} f_{nm}^{t}(r)\boldsymbol{Y}_{n,n}^{m}(\theta,\phi)}_{\boldsymbol{B}^t(\boldsymbol{r})} + \underbrace{\sum_{n=1}^{\infty}\sum_{m=-n}^{n} \nabla \times [f_{nm}^{p}(r)\boldsymbol{Y}_{n,n}^{m}(\theta,\phi)]}_{\boldsymbol{B}^p(\boldsymbol{r})}, \tag{5}$$

where f_{nm}^t and f_{nm}^p are scalar functions that could further be expanded in some basis. $\boldsymbol{B}^t$ and $\boldsymbol{B}^p$ are the toroidal and poloidal parts of $\boldsymbol{B}$, respectively. Requiring that $\nabla \times \boldsymbol{B}(\boldsymbol{r}) = \mu_0 \boldsymbol{J}_V(\boldsymbol{r})$, when $r \neq r_Q$, gives us a system of three equations, which can be used to solve f_{nm}^t and f_{nm}^p. According to Eqs. (A4) and (A7), $\nabla \times \boldsymbol{B}^p$ has no radial component; thus, we can find f_{nm}^t from $\boldsymbol{e}_r \cdot (\nabla \times \boldsymbol{B}^t - \mu_0 \boldsymbol{J}_V) = 0 \iff \boldsymbol{e}_r \cdot (\nabla \times \boldsymbol{B}^t - \mu_0 \boldsymbol{\sigma} \circ \boldsymbol{E}) = 0$, when $r \neq r_Q$. Using Eqs. (2), (5), (A3), (A5), and (A6), we get

$$f_{nm}^t(r) = \mu_0 \sigma_{r,k} Q_n^m(\boldsymbol{r}_Q)\left(\sqrt{\frac{n}{n+1}}\frac{v_{k,n}}{n} r^{v_{k,n}} a_{\xi,k,n} + -\sqrt{\frac{n+1}{n}}\frac{v_{k,n}+1}{n+1} r^{-(v_{k,n}+1)} b_{\xi,k,n}\right), \tag{6}$$

when $r_{k-1} < r < r_k$ and $r \neq r_Q$. By a substitution of Eqs. (B3) and (6), we find that $\nabla \times \boldsymbol{B}^t = \mu_0 \boldsymbol{J}_V$, when $r \neq r_Q$. Thus, $\nabla \times \boldsymbol{B}^p = 0$, when $r \neq r_Q$. We now proceed to find a closed-form expression for $\boldsymbol{B}^p$.

Reference 32 shows that, for a layered spherically symmetric isotropic conductor, the radial component of the magnetic field due to a current dipole can be calculated from the primary current density without considering the volume current density. Reference 33 generalizes the result for anisotropic conductivity by showing that the radial component of the external or internal magnetic field is not influenced by a difference between radial and tangential conductivity. Because $\nabla \times \boldsymbol{B}^p = 0$ when $r \neq r_Q$, there exists a magnetic scalar potential U so that $\boldsymbol{B}^p(\boldsymbol{r}) = -\mu_0 \nabla U(\boldsymbol{r})$, when $r \neq r_Q$. Because the volume currents do not contribute to the radial component of the magnetic field, the radial field component for a current dipole $\boldsymbol{J}_P(\boldsymbol{r}) = \boldsymbol{Q}\delta(\boldsymbol{r} - \boldsymbol{r}_Q)$ is obtained using the Biot–Savart law as

$$B_{Q,r}(\boldsymbol{r}) = \frac{\mu_0}{4\pi}\frac{\boldsymbol{Q} \times (\boldsymbol{r} - \boldsymbol{r}_Q)}{|\boldsymbol{r} - \boldsymbol{r}_Q|^3} \cdot \boldsymbol{e}_r = -\frac{\mu_0}{4\pi}\frac{\boldsymbol{Q} \times \boldsymbol{r}_Q \cdot \boldsymbol{e}_r}{|\boldsymbol{r} - \boldsymbol{r}_Q|^3}. \tag{7}$$

As seen from Eqs. (5) and (A4), because $\boldsymbol{e}_r \cdot \boldsymbol{B}^t = 0$, $\boldsymbol{e}_r \cdot \boldsymbol{B}^p = \boldsymbol{e}_r \cdot \boldsymbol{B} = B_{Q,r}$.

In order to find U, we utilize the technique which was used in Ref. 14 to obtain the magnetic field outside a spherically symmetric conductor due to a current dipole inside. When $r < r_Q$, we can find U as a line integral of ∇U along a radial path starting from the origin. By choosing U to vanish at the origin, we obtain

$$\begin{aligned} U(\boldsymbol{r}) &= \int_0^r \nabla U(t\boldsymbol{e}_r) \cdot \boldsymbol{e}_r dt = -\frac{1}{\mu_0}\int_0^r B_{Q,r}(t\boldsymbol{e}_r) dt \\ &= \frac{\boldsymbol{Q} \times \boldsymbol{r}_Q \cdot \boldsymbol{e}_r}{4\pi}\int_0^r \frac{1}{|t\boldsymbol{e}_r - \boldsymbol{r}_Q|^3} dt \\ &= -\frac{1}{4\pi}\frac{\boldsymbol{Q} \times \boldsymbol{r}_Q \cdot \boldsymbol{r}}{F(\boldsymbol{r})}, \quad r < r_Q, \end{aligned} \tag{8}$$

where

$$F(\boldsymbol{r}) = -\frac{r_Q a}{a + r_Q}\left(r_Q a + r_Q^2 - \boldsymbol{r}_Q \cdot \boldsymbol{r}\right), \quad r < r_Q \tag{9}$$

and $\boldsymbol{a} = \boldsymbol{r} - \boldsymbol{r}_Q$. Finally, we calculate $\boldsymbol{B}^p$ using ∇U:

$$\boldsymbol{B}^p(\boldsymbol{r}) = \frac{\mu_0}{4\pi F^2}(F\boldsymbol{Q} \times \boldsymbol{r}_Q - \boldsymbol{Q} \times \boldsymbol{r}_Q \cdot \boldsymbol{r}\nabla F), \tag{10}$$

where

$$\begin{aligned} \nabla F(\boldsymbol{r}) = &\frac{r_Q^2\left(a^2/r_Q - \boldsymbol{a} \cdot \boldsymbol{r}_Q/a + 2a + 2r_Q\right)}{(a + r_Q)^2}\boldsymbol{r}_Q + \\ &-\frac{r_Q^2\left(a + 2r_Q - \boldsymbol{a} \cdot \boldsymbol{r}_Q/a\right)}{(a + r_Q)^2}\boldsymbol{r}, \quad r < r_Q. \end{aligned} \tag{11}$$

When $r > r_Q$, we can apply the result of Ref. 14, i.e., the Sarvas formula, directly: $\boldsymbol{B}^p$ is given by Eq. (10) but with the following expressions for F and ∇F:

$$F(\boldsymbol{r}) = a(ra + r^2 - \boldsymbol{r}_Q \cdot \boldsymbol{r}), \quad r > r_Q, \tag{12}$$

$$\begin{aligned} \nabla F(\boldsymbol{r}) = &(a^2/r + \boldsymbol{a} \cdot \boldsymbol{r}/a + 2a + 2r)\boldsymbol{r} + \\ &-(a + 2r + \boldsymbol{a} \cdot \boldsymbol{r}/a)\boldsymbol{r}_Q, \quad r > r_Q. \end{aligned} \tag{13}$$

Collecting the results, we obtain the following form for the magnetic field inside the spherical conductor (when $r \neq r_Q$):

$$\begin{aligned} \boldsymbol{B}(\boldsymbol{r}) = &\mu_0 \sigma_{r,k}\sum_{n=1}^{\infty}\sum_{m=-n}^{n} Q_n^m(\boldsymbol{r}_Q)\left(\sqrt{\frac{n}{n+1}}\frac{v_{k,n}}{n} r^{v_{k,n}} a_{\xi,k,n} + \right. \\ &\left. -\sqrt{\frac{n+1}{n}}\frac{v_{k,n}+1}{n+1} r^{-(v_{k,n}+1)} b_{\xi,k,n}\right)\boldsymbol{Y}_{n,n}^m(\theta,\phi) \\ &+ \boldsymbol{B}^p(\boldsymbol{r}), \quad r_{k-1} \leq r \leq r_k. \end{aligned} \tag{14}$$

Outside the conductor, $\boldsymbol{B}^t = 0$ and the magnetic field is given by Eq. (10). More generally, $\boldsymbol{B}^p$ can be considered the magnetic field in a zero-conductivity region. In regions with non-zero conductivity and current density, $\boldsymbol{B}^t$ acts as a correction term. In Appendix D, we show that, for large n, the terms in the series of Eq. (14) scale as $(r/r_Q)^n$ and $(r_Q/r)^{n+1}$, when $r < r_Q$ and $r > r_Q$, respectively. Note that when Eq. (14) is implemented as such, the computations are suspect to

numerical overflow and underflow problems; in our implementation, we avoided them by expressing the radial coordinates and the layer radii as ratios.[20,34]

3. Addition–subtraction method

In order to obtain a solution with a convergence better than that of Eq. (14) when $r \approx r_\mathrm{Q}$, we use an addition–subtraction strategy similar to the one presented in Ref. 20 for the electric potential. Here, the idea is to subtract a series from and to add its closed-form solution to Eq. (14). If the subtracted series and Eq. (14) have a similar behavior for large n, the resulting series convergences faster than the original. Here, we use the closed-form solution of the magnetic field inside an isotropic homogeneous sphere[17] and the respective series expression, Eq. (14), to achieve this goal. The closed-form solution, $\boldsymbol{B}^\mathrm{cf}_\mathrm{homog}$, is presented in Appendix E, and the series-form expression, $\boldsymbol{B}^\mathrm{sf}_\mathrm{homog}$, can be obtained using Eq. (14) by applying it to a homogeneous sphere.

Mathematically, the addition–subtraction solution can be written as follows:

$$\begin{aligned}\boldsymbol{B}(\boldsymbol{r}) &= \boldsymbol{B}(\boldsymbol{r}) - w_{\xi,k}\boldsymbol{B}^\mathrm{sf}_\mathrm{homog}(\boldsymbol{r}) + w_{\xi,k}\boldsymbol{B}^\mathrm{cf}_\mathrm{homog}(\boldsymbol{r}),\\ &r_{k-1} \le r \le r_k, \quad r \neq r_\mathrm{Q},\end{aligned} \tag{15}$$

where the needed weights, $w_{\xi,k}$, are solved by requiring that on the right-hand side of Eq. (15) the terms with the poorest convergence cancel out for large n. The result is obtained by computing the ratio of the series terms in $\boldsymbol{B}$ and $\boldsymbol{B}^\mathrm{sf}_\mathrm{homog}$ for large n. The asymptotic behavior of the series terms is derived in Appendix D and given by Eqs. (D7) and (D8). First, let us consider the case $r < r_\mathrm{Q}$ ($\xi = 0$):

$$\begin{aligned}w_{0,k} &= \frac{\sigma_{\mathrm{rt},k}}{\sigma_{\mathrm{rt},1}}\frac{a_{0,k,n}b_{1,k_\mathrm{Q},n}}{b_{1,1,n}} r^{v_{k,n}-n} r_\mathrm{Q}^{n-v_{k_\mathrm{Q},n}}\\ &= \frac{\sigma_{\mathrm{rt},k}}{\sigma_{\mathrm{rt},1}}\frac{\prod_{i=1}^{k-1}\frac{1}{2}\left(1+\frac{\sigma_{\mathrm{rt},i}}{\sigma_{\mathrm{rt},i+1}}\right)}{\prod_{i=1}^{k_\mathrm{Q}-1}\frac{1}{2}\left(1+\frac{\sigma_{\mathrm{rt},i+1}}{\sigma_{\mathrm{rt},i}}\right)}\frac{r^{v_{k,n}-n} r_\mathrm{Q}^{n-v_{k_\mathrm{Q},n}}}{\prod_{i=k}^{k_\mathrm{Q}-1} r_i^{v_{i,n}-v_{i+1,n}}}\\ &= \frac{1}{\prod_{i=k}^{k_\mathrm{Q}-1}\frac{1}{2}\left(1+\frac{\sigma_{\mathrm{rt},i+1}}{\sigma_{\mathrm{rt},i}}\right)}\frac{r^{v_{k,n}-n} r_\mathrm{Q}^{n-v_{k_\mathrm{Q},n}}}{\prod_{i=k}^{k_\mathrm{Q}-1} r_i^{v_{i,n}-v_{i+1,n}}},\\ &r_{k-1} \le r \le r_k, r \neq r_\mathrm{Q},\end{aligned} \tag{16}$$

where we have defined $\sigma_{\mathrm{rt},i} = \sqrt{\sigma_{\mathrm{r},i}\sigma_{\mathrm{t},i}}$. We note that in order to have an n-independent $w_{0,k}$, the layers containing the dipole and the field point, and all layers in between, must be isotropic (i.e., $v_i = n, i = k, k+1, \ldots, k_\mathrm{Q}$). In this case,

$$w_{0,k} = \frac{1}{\prod_{i=k}^{k_\mathrm{Q}-1}\frac{1}{2}\left(1+\frac{\sigma_{\mathrm{rt},i+1}}{\sigma_{\mathrm{rt},i}}\right)}, \quad r_{k-1} \le r \le r_k, \quad r \neq r_\mathrm{Q}. \tag{17}$$

Next, for $r > r_\mathrm{Q}$ ($\xi = 1$),

$$\begin{aligned}w_{1,k} &= \frac{\sigma_{\mathrm{rt},k}}{\sigma_{\mathrm{rt},1}}\frac{a_{0,k_\mathrm{Q},n}b_{1,k,n}}{b_{1,1,n}} r^{n-v_{k,n}} r_\mathrm{Q}^{v_{k_\mathrm{Q},n}-n}\\ &= \frac{\sigma_{\mathrm{rt},k}}{\sigma_{\mathrm{rt},1}}\frac{\prod_{i=1}^{k_\mathrm{Q}-1}\frac{1}{2}\left(1+\frac{\sigma_{\mathrm{rt},i}}{\sigma_{\mathrm{rt},i+1}}\right)}{\prod_{i=1}^{k-1}\frac{1}{2}\left(1+\frac{\sigma_{\mathrm{rti}+1}}{\sigma_{\mathrm{rt},i}}\right)}\frac{r^{n-v_{k,n}} r_\mathrm{Q}^{v_{k_\mathrm{Q},n}-n}}{\prod_{i=k_\mathrm{Q}}^{k-1} r_i^{v_{i,n}-v_{i+1,n}}}\\ &= \frac{1}{\prod_{i=k_\mathrm{Q}}^{k-1}\frac{1}{2}\left(1+\frac{\sigma_{\mathrm{rt},i}}{\sigma_{\mathrm{rt},i+1}}\right)}\frac{r^{n-v_{k,n}} r_\mathrm{Q}^{v_{k_\mathrm{Q},n}-n}}{\prod_{i=k_\mathrm{Q}}^{k-1} r_i^{v_{i,n}-v_{i+1,n}}},\\ &r_{k-1} \le r \le r_k, \quad r \neq r_\mathrm{Q}.\end{aligned} \tag{18}$$

Similarly to the $\xi = 0$ case, we need to have isotropic conductivity between the source and the field point (i.e., $v_i = n, i = k_\mathrm{Q}, k_\mathrm{Q}+1, \ldots, k$) in order to make the n in Eq. (18) vanish. This yields

$$w_{1,k} = \frac{1}{\prod_{i=k_\mathrm{Q}}^{k-1}\frac{1}{2}\left(1+\frac{\sigma_{\mathrm{rt},i}}{\sigma_{\mathrm{rt},i+1}}\right)}, \quad r_{k-1} \le r \le r_k, r \neq r_\mathrm{Q}. \tag{19}$$

B. Simulations

1. Convergence and verification

In addition to the theoretical inspection presented in Appendix D, we also analyzed the convergence of Eqs. (14) and (15) by calculating the magnetic field for 1000 random line–dipole pairs: First, we sampled 1000 dipole positions $[r_{\mathrm{Q},i}, \theta_{\mathrm{Q},i}, \phi_{\mathrm{Q},i}]$ ($i = 1, \ldots, 1000$), where $\theta_{\mathrm{Q},i}$ and $\phi_{\mathrm{Q},i}$ were randomized and $r_{\mathrm{Q},i} = 68$ mm. For each position, the dipole orientation was chosen randomly. Second, for each dipole we sampled a random radial line, with its orientation given by (θ_i, ϕ_i), on which the magnetic field was computed. The conductivity model used in the analysis was the five-layer anisotropic spherical head model described in Sec. II B 2. We calculated the truncation error as

$$\varepsilon_N(r) = \max_i \frac{|\boldsymbol{B}_N(r,\theta_i,\phi_i) - \boldsymbol{B}_{500}(r,\theta_i,\phi_i)|}{|\boldsymbol{B}_{500}(r,\theta_i,\phi_i)|}, \tag{20}$$

where $\boldsymbol{B}_N(r,\theta_i,\phi_i)$ refers to the magnetic field on the ith line for the ith dipole when the summation over n in Eq. (14) was truncated at $n = N$. The reference, $\boldsymbol{B}_{500}$, was always computed using the addition–subtraction method. In addition, we studied the performance of the addition–subtraction method in models with up to 1 000 000-fold conductivity differences between the layers confirming that the method is not sensitive to the properties of the layers, and thus the approach is valid beyond the case of human head (data not shown).

We also verified Eqs. (14) and (15) and their implementation by computing internal magnetic fields due to a set of dipoles in a four-layer isotropic geometry and comparing the results with those computed using our previously verified boundary-element method (BEM) solver;[28] see Sec. II B 2 for radii and conductivities of the layers. We generated four topologically identical regularly positioned meshes that had 5120 triangles per boundary surface. The radii of the meshes

were scaled so that the surface areas of the true and triangulated spheres were the same. For this anatomical model, we built volume conductor model using linear Galerkin BEM formulated with isolated source approach.[28] For each dipole, this model gives the electric potential on each boundary surface, from which the contribution of the volume current density to the total magnetic field inside the sphere is computed using the Geselowitz integral formula.[32] For more details and some previous verifications, see Ref. 28. The analytical solutions were calculated by truncating the series in Eq. (14) at $n = 250$. Similar to the convergence analysis described above, we sampled 1000 random line–dipole pairs. The comparison was done separately for two source depths with the dipoles located at $r_Q = 35$ mm and $r_Q = 68$ mm, respectively. In both cases, we computed the relative error between the magnetic field amplitudes $(1 - |\boldsymbol{B}_{\text{series}}|/|\boldsymbol{B}_{\text{BEM}}|)$ and the difference in the magnetic field direction for all field-point locations. We assessed the results as a function of field-point depth by taking the median and 1st and 99th percentiles of the metrics at each depth. To avoid errors due to discretization of boundary potentials in the BEM, we omitted the field points that were closer than 1 mm (approximately 1/5–1/6 of the triangle side length) from any boundary.

2. Examples

We studied the effect of the radially varying conductivity on the magnetic field produced by a current dipole. Our most detailed model was an anisotropic five-layer spherical head model centered at the origin. The compartments modeled white and gray matter, CSF, skull, and scalp with their outer radii set to $[0.65, 0.90, 0.92, 0.97, 1] \times 80$ mm. We evaluated also three different isotropic spherical head models:

a. Four-layer model: The outer radii of the layers (brain, CSF, skull, and scalp) were set to $[0.90, 0.92, 0.97, 1] \times 80$ mm.

b. Three-layer model: The outer radii of the layers (brain, skull, and scalp) were set to $[0.92, 0.97, 1] \times 80$ mm.

c. Homogeneous-sphere model: The radius of the sphere modeling the intracranial cavity was set to 73.6 mm. In this model, the calculations were done using the closed-form formula Eq. (E1) of Ref. 17.

The conductivities of the isotropic compartments were $\sigma_{\text{brain}} = \sigma_{\text{scalp}} = 0.33\,\text{S/m}$, $\sigma_{\text{CSF}} = 1.8\,\text{S/m}$ (Ref. 35), and $\sigma_{\text{skull}} = 8.3\,\text{mS/m}$. In the five-layer model, the white matter and the skull were assumed anisotropic. Their radial and tangential conductivities were set to $\sigma_{\text{r, white matter}} = 2\sigma_{\text{t, white matter}} = 6\sigma_{\text{brain}}/4$ and $\sigma_{\text{t, skull}} = 2\sigma_{\text{r, skull}} = 6\sigma_{\text{skull}}/5$. These choices are approximately in line with the values suggested in the literature,[36–38] while preserving the same average value of conductivity as in the isotropic models; thus the difference in results is due to the effect of anisotropy only. In the five-layer model, the conductivities of the CSF and the scalp were the same as in the other models; the conductivity of the gray matter was set to $\sigma_{\text{gray matter}} = \sigma_{\text{brain}}$.

With each model, we computed the magnetic field produced by a radial ($\boldsymbol{Q} = Q\boldsymbol{e}_r$) and tangential ($\boldsymbol{Q} = Q\boldsymbol{e}_\phi$) current dipole located in the xy plane at $\boldsymbol{r}_Q = [r_Q, \theta_Q, \phi_Q] = [68\,\text{mm}, \pi/2, 0]$ with $Q = 10$ nAm. In all layered models, we used the addition–subtraction method in Eq. (15) and truncated the summation in Eq. (14) at $n = 250$. The calculations were performed with Mathematica (Wolfram Research, Inc., Champaign, IL, USA).

III. RESULTS

A. Convergence and verification

Figure 2 illustrates the convergence of Eq. (14) computed with and without the addition–subtraction method as described in Sec. II B 1. As expected from the asymptotic behavior of Eq. (14), without the addition–subtraction method, the magnetic field converges slowly when $r \approx r_Q$. On the other hand, when using the addition–subtraction method, the relative error stays below 1% everywhere with about 250 terms. Because the white matter and skull are anisotropic, we used the addition–subtraction method to improve the convergence only within the gray-matter and CSF layers, in order to comply with the isotropicity requirements of Eqs. (17) and (19).

In Fig. 3, we present the results of our BEM verification. The overall match between the BEM and series solutions is excellent; this indicates that the derived expressions are correct. Only near the conductivity boundaries, the results obtained with BEM and the analytical expression differ slightly. This is likely due to both the discretization error of the volume currents in BEM and the truncation of the analytical solution.

B. Examples

In Figs. 4 and 5, we show magnetic field maps in the xy plane for the radial and tangential current dipoles using the four different spherical head models.

Let us first discuss the field maps produced by the tangential current dipole. As expected, because of the poorly conducting skull, in the skull and scalp layers, the magnetic fields of the different models show only minor differences. For the same reason, the homogeneous-sphere model and the three-layer model give highly similar magnetic field maps also in the brain. The main difference between the three- and four-layer models (and the homogeneous-sphere and the four-layer models) is that, in the four-layer model, the CSF compartment, which is relatively well-conductive, attracts current and causes a notable change in the magnetic field (Fig. 5). The effect of the anisotropy present in the five-layer model is most easily seen in the white-matter region, where the current flow prefers the radial direction and the magnetic field changes accordingly (Fig. 4). However, as the modeled anisotropy is not that high (2:1) and the white-matter boundary is relatively far from the source dipole, the four- and five-layer models produce otherwise quite similar field maps. For stronger anisotropy or a source closer to or within an anisotropic layer, the difference is larger (data not shown).

With the radial current dipole, the main difference between the homogeneous-sphere model and the three- and four-layer models is that in the former the magnetic field is confined to the intracranial cavity, whereas in the layered models the magnetic field penetrates the skull boundary. However, as required by the spherically symmetric

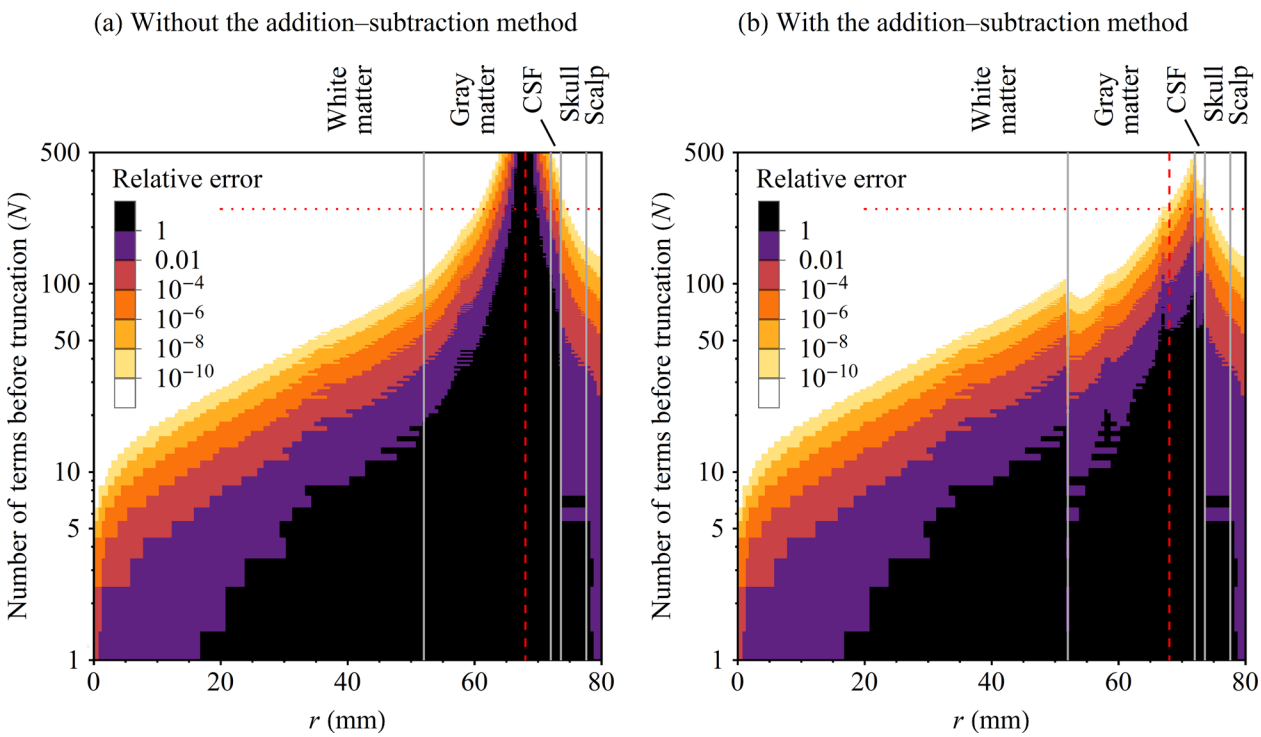

FIG. 2. Convergence of the magnetic field according to Eq. (20) as a function of the number of terms N in the summation over n in Eq. (14). The relative error is visualized using a logarithmic color scale. (a) and (b) show the convergence without and with the addition–subtraction method of Eq. (15), respectively. The red dashed vertical line indicates the position of the current dipole. The solid gray lines indicate the layer boundaries. The red horizontal dotted line marks $N = 250$.

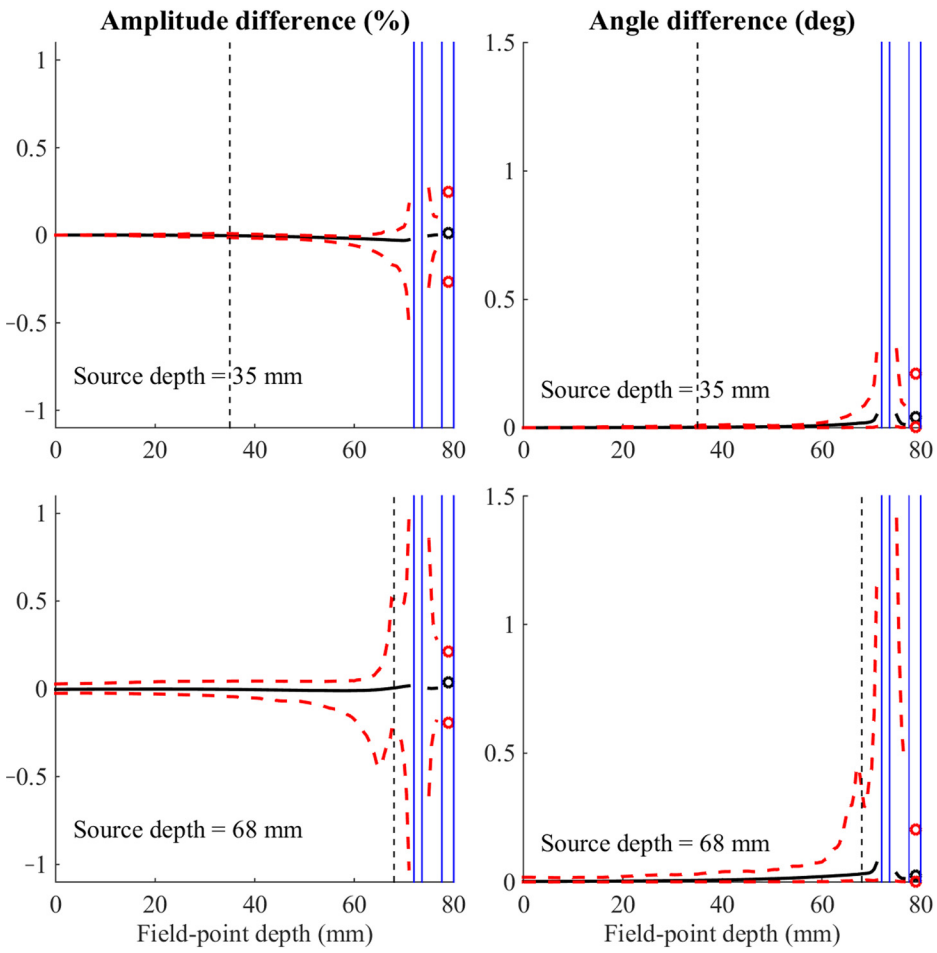

FIG. 3. Comparison between the analytical and BEM calculations for two source depths. The black lines show the median values, and the dashed red curves give the 1st and 99th percentiles of the data. The dipole positions are marked by the dashed vertical lines; the layer boundaries are indicated by the blue vertical lines.

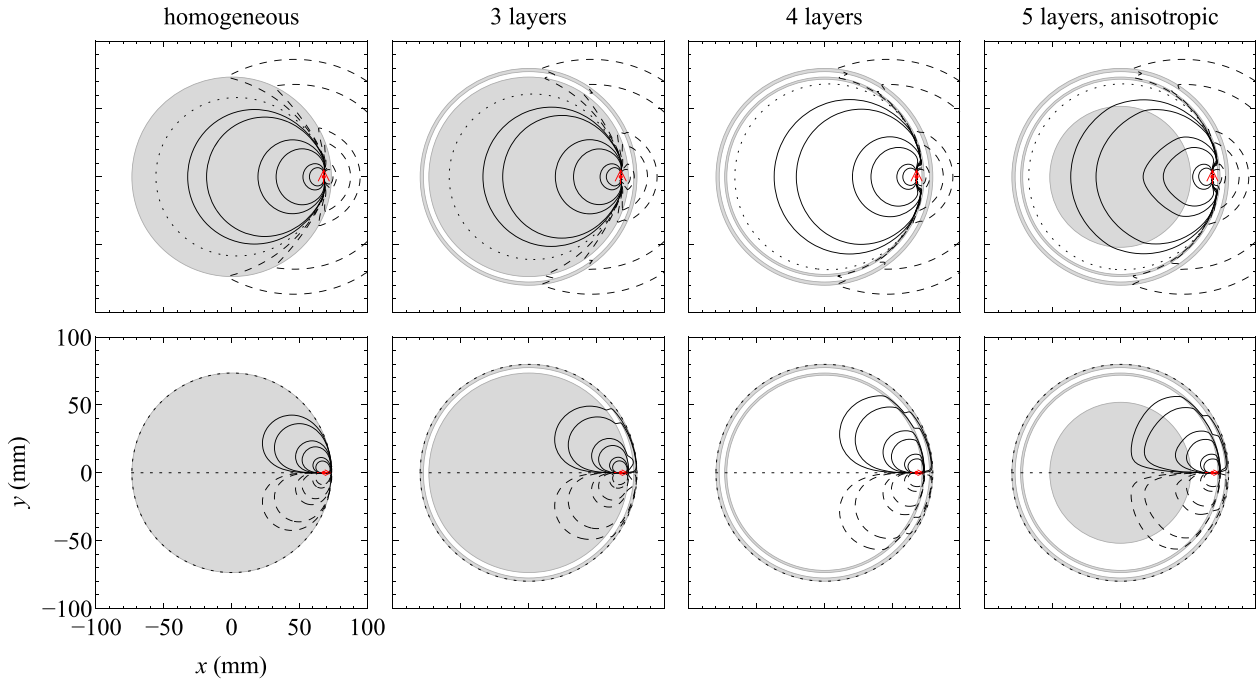

FIG. 4. The z component of the magnetic field in the xy plane for the tangential (top) and radial (bottom) dipole using the homogeneous-sphere model (first column), the three-layer model (second column), the four-layer model (third column), and the anisotropic five-layer model (fourth column). The contour lines are drawn at 0, ±0.05, ±0.1, ±0.5, ±1, ±5, and ±10 pT. Positive and negative contours are indicated by solid and dashed lines, respectively. The zero contours are shown with dotted lines. The conductivity structure of the sphere is illustrated by plotting every other layer in gray. The dipole positions and orientations are indicated by the red dots and arrows, respectively.

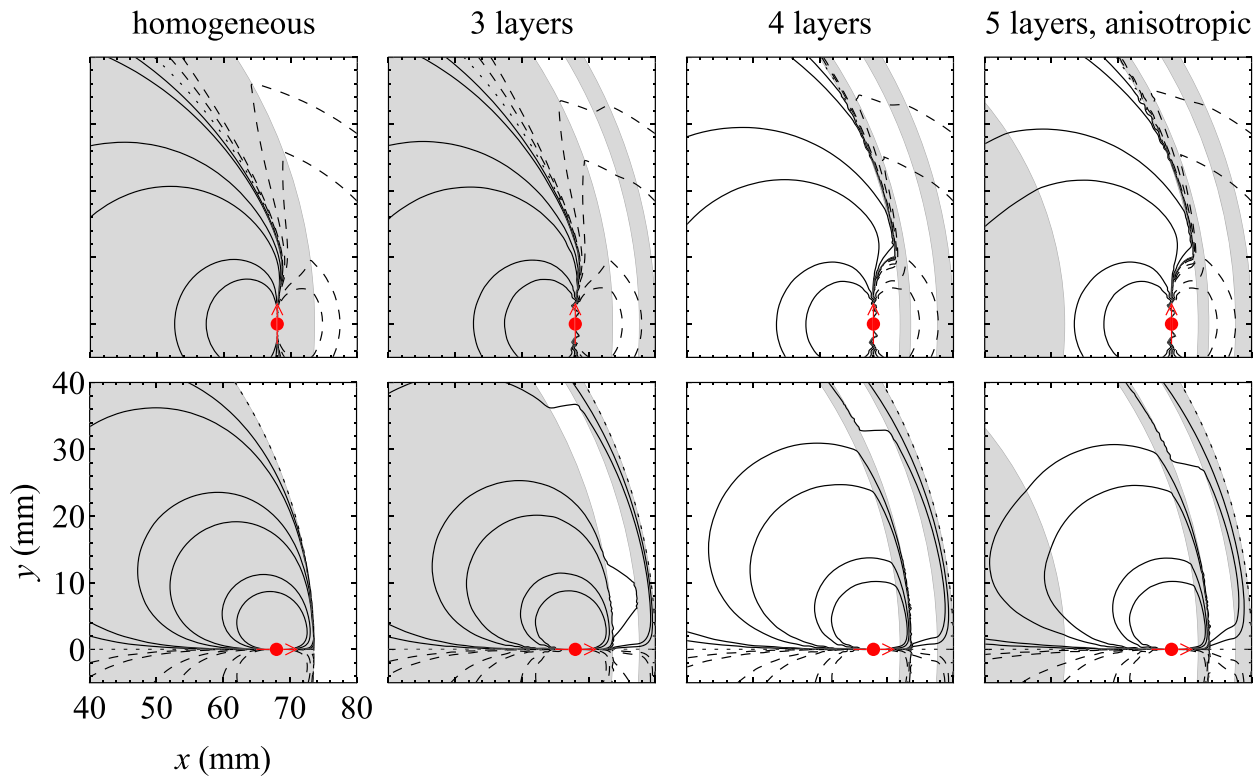

FIG. 5. The z component of the magnetic field in the xy plane around the dipole location for the tangential (top) and radial (bottom) dipole using the four different spherical head models. The contour lines are drawn at 0, ±0.05, ±0.1, ±0.5, ±1, ±5, and ±10 pT. Positive and negative contours are indicated by solid and dashed lines, respectively. The zero contours are shown with dotted lines. The conductivity structure of the sphere is illustrated by plotting every other layer in gray. The dipole positions and orientations are indicated by the red dots and arrows, respectively.

conductor geometry, also in the layered models, the field outside the conductor is zero. The other aspects of the field-map differences reflect those of the tangential current dipole. Comparing the plots of the radial and tangential current dipoles reveals that the magnetic field due to the radial current dipole is more focal.

IV. DISCUSSION

The presented results indicate that the differences between the homogeneous-sphere model and the studied three-layer model are really small, as the poorly conductive skull is, for the present purposes, effectively an insulator. This result is in agreement with the discussion presented in Ref. 17. The addition of a well conductive CSF layer between the brain matter and the skull introduces, however, some notable differences. This result also suggests that, for accurate modeling of the magnetic field inside the head for sources near the CSF boundary, it is necessary to have a model of the CSF compartment.

Compared with BEM, an advantage of the present analytical model is that anisotropic layers can be included in the computations. Although Fig. 4 shows only minor differences between the isotropic four-layer model and the anisotropic five-layer model, the modeling of the anisotropy becomes more important when there are layers with stronger anisotropy or the source is closer to or within an anisotropic layer.

In DNI, the ultimate goal is not to image the magnetic field inside the head but to locate the source currents, or the neuronal activity, producing it. Thus, when mapping of the neuronal magnetic field inside the head becomes feasible, the presented multilayer model may enhance the reconstruction of the primary current density in DNI compared with the homogeneous-sphere model.

In our case, we had a spherical conductor in free space, as our motivation was brain imaging. However, the approach of this study suits equally well for calculating the magnetic field in an unbounded spherically symmetric medium. Furthermore, the conductor may contain, e.g., a nonconductive spherical cavity in its center. Although we only considered the field due to a single current dipole, the internal magnetic field due to a more general source current density can be obtained from elementary source dipoles using superposition.

In addition to being a useful modeling tool, the derived analytical expression for the magnetic field can serve as means to assess numerical methods: implementations of BEM or the finite-element (FEM) or finite-difference (FDM) method for magnetic field computations can now be verified also inside layered spherical conductors. This can be especially useful for assessing the validity of approximations that are carried out in FEM or FDM modeling when representing focal dipolar sources. For example, a dipolar source is in FEM EEG/MEG studies often represented using St. Venant approach,[39,40] in which the dipole is approximated by a set of monopoles in nearest nodes of the mesh, aiming at the correct dipole moment. This approach can only be valid far from the dipole. To compute magnetic fields close to the source, other approaches such as full subtraction or partial integration[27] need to be verified and applied. A related application is the optimization of the volume/boundary meshing close to the sources. This can be especially useful in the case of FEM and anisotropic white matter.[13]

V. CONCLUSION

In this paper, we derived an expression for the magnetic field inside a multilayer spherically symmetric anisotropic conductor due to an internal current dipole. We demonstrated the use of the obtained formula by studying the effect of the radially varying conductivity on the magnetic field produced by a current dipole. The results showed that the solution obtained using the multilayer model may, depending on the relative conductivities, differ from that given by the homogeneous-sphere model. A Mathematica implementation of Eqs. (14) and (15) is available from "Jaakko O. Nieminen."

ACKNOWLEDGMENTS

The authors thank Risto Ilmoniemi for useful comments on the manuscript. The research has received funding from the Academy of Finland (Decisions No. 255347 and 265680).

APPENDIX A: VECTOR SPHERICAL HARMONICS

This Appendix presents the different spherical harmonics used in this paper. Following, e.g., Ref. 41, the real spherical harmonics Y are here defined as

$$Y_n^m(\theta,\phi)=\begin{cases}\sqrt{\dfrac{(2n+1)(n-m)!}{2\pi(n+m)!}}P_n^m(\cos\theta)\cos m\phi, & m>0\\ \sqrt{\dfrac{2n+1}{4\pi}}P_n^0(\cos\theta), & m=0\\ -\sqrt{\dfrac{(2n+1)(n+m)!}{2\pi(n-m)!}}P_n^{-m}(\cos\theta)\sin m\phi, & m<0,\end{cases} \tag{A1}$$

where P_n^m are associated Legendre functions.[42] These functions are orthonormal over the sphere:

$$\int_0^{2\pi}\int_0^{\pi} Y_n^m(\theta,\phi)Y_{n'}^{m'}(\theta,\phi)\sin\theta d\theta d\phi=\delta_{nn'}\delta_{mm'}. \tag{A2}$$

In this study, we use the following definition of real vector spherical harmonics $\boldsymbol{Y}$:

$$\boldsymbol{Y}_{n,n+1}^m(\theta,\phi)=\frac{1}{\sqrt{(n+1)(2n+1)}}r^{n+2}\nabla\left[\frac{1}{r^{n+1}}Y_n^m(\theta,\phi)\right], \tag{A3}$$

$$\boldsymbol{Y}_{n,n}^m(\theta,\phi)=\frac{1}{\sqrt{n(n+1)}}\boldsymbol{r}\times\nabla Y_n^m(\theta,\phi), \tag{A4}$$

$$\boldsymbol{Y}_{n,n-1}^m(\theta,\phi)=\frac{1}{\sqrt{n(2n+1)}}\frac{1}{r^{n-1}}\nabla\left[r^nY_n^m(\theta,\phi)\right]. \tag{A5}$$

The definition follows that of the complex vector spherical harmonics introduced in Refs. 43 and 44. The vector spherical harmonics form a complete set suitable for presenting any vector function on the surface of a sphere. As seen directly from the definition, $\boldsymbol{Y}^m_{n,n}$ has no radial component. Also the following properties of the vector spherical harmonics are used in this paper:

$$\nabla \times \left(f(r)\boldsymbol{Y}^m_{n,n}\right) = \sqrt{\frac{n}{2n+1}}\left(\frac{n}{r} - \frac{\partial}{\partial r}\right) f\boldsymbol{Y}^m_{n,n+1} + \\ -\sqrt{\frac{n+1}{2n+1}}\left(\frac{n+1}{r} + \frac{\partial}{\partial r}\right) f\boldsymbol{Y}^m_{n,n-1} \quad \text{(A6)}$$

and

$$\nabla \times \left(\nabla \times f(r)\boldsymbol{Y}^m_{n,n}\right) = \left(\frac{n(n+1)}{r^2} - \frac{2}{r}\frac{\partial}{\partial r} - \frac{\partial^2}{\partial r^2}\right) f\boldsymbol{Y}^m_{n,n}, \quad \text{(A7)}$$

where $f(r)$ is a scalar function. Many other identities for the real vector spherical harmonics follow from those given in Ref. 44.

Any divergence-free real-valued vector field in a volume can be presented as a linear combination of the basis functions

$$\boldsymbol{u}_{nm}(r,\theta,\phi) = f^{\mathrm{t}}_{nm}(r)\boldsymbol{Y}^m_{n,n}(\theta,\phi) + \nabla \times [f^{\mathrm{p}}_{nm}(r)\boldsymbol{Y}^m_{n,n}(\theta,\phi)], \quad \text{(A8)}$$

where f^{t}_{nm} and f^{p}_{nm} are scalar functions.[45] The first and second terms on the right-hand side of Eq. (A8) are basis functions for the toroidal and poloidal fields (according to the toroidal–poloidal decomposition[31]), respectively. Although not explicitly written here, f^{t}_{nm} and f^{p}_{nm} can further be expressed using a complete set of scalar basis functions.

APPENDIX B: ELECTRIC POTENTIAL

Here, we present the solution of Refs. 19 and 22 for the electric potential, V, inside a spherically symmetric conductor due to an internal quasi-static current dipole. We write V using real spherical harmonics Y and real vector spherical harmonics $\boldsymbol{Y}$ (see Appendix A for their definitions):

$$V(\boldsymbol{r}) = \sum_{n=0}^{\infty}\sum_{m=-n}^{n} Q^m_n(\boldsymbol{r}_{\mathrm{Q}})\left(a_{\xi,k,n}r^{v_{k,n}} + b_{\xi,k,n}r^{-(v_{k,n}+1)}\right)Y^m_n(\theta,\phi), \\ r_{k-1} \le r \le r_k, \quad \text{(B1)}$$

where

$$Q^m_n(\boldsymbol{r}_{\mathrm{Q}}) = \frac{\sqrt{2n+1}\boldsymbol{Q}}{(2v_{1,n}+1)\sigma_{\mathrm{r},1}b_{1,1,n}} \\ \cdot\left\{a_{1-\xi,k_{\mathrm{Q}},n}\sqrt{n}\times r_{\mathrm{Q}}^{v_{k_{\mathrm{Q}},n}-1}\left[\frac{v_{k_{\mathrm{Q}},n}}{n},1,1\right]\circ\boldsymbol{Y}^m_{n,n-1}(\theta_{\mathrm{Q}},\phi_{\mathrm{Q}})\right. \\ +b_{1-\xi,k_{\mathrm{Q}},n}\sqrt{n+1}r_{\mathrm{Q}}^{-\left(v_{k_{\mathrm{Q}},n}+2\right)} \\ \left.\times\left[\frac{v_{k_{\mathrm{Q}},n}+1}{n+1},1,1\right]\circ\boldsymbol{Y}^m_{n,n+1}(\theta_{\mathrm{Q}},\phi_{\mathrm{Q}})\right\}, \quad \text{(B2)}$$

$$v_{k,n} = \sqrt{n(n+1)\sigma_{\mathrm{t},k}/\sigma_{\mathrm{r},k} + 1/4} - 1/2 \quad \text{(B3)}$$

(for isotropic layers, $v_{k,n} = n$), the dipole is located in the compartment k_{Q}, i.e., $r_{k_{\mathrm{Q}}-1} < r_{\mathrm{Q}} < r_{k_{\mathrm{Q}}}$, and ξ serves the purpose of separating the spherical volume into two regions: $\xi = 0$, when $r < r_{\mathrm{Q}}$, and $\xi = 1$, when $r > r_{\mathrm{Q}}$. With the help of ξ, we avoid the burden of writing separate equations for the regions $r < r_{\mathrm{Q}}$ and $r > r_{\mathrm{Q}}$. The coefficients $a_{\xi,k,n}$ and $b_{\xi,k,n}$ are defined recursively:

$$\begin{bmatrix} a_{\xi,k+1,n} \\ b_{\xi,k+1,n} \end{bmatrix} = \mathbf{C}^{-1}_{k+1,n}(r_k)\mathbf{C}_{k,n}(r_k)\begin{bmatrix} a_{\xi,k,n} \\ b_{\xi,k,n} \end{bmatrix}, \quad \text{(B4)}$$

where

$$\mathbf{C}_{k,n}(r) = \begin{bmatrix} r^{v_{k,n}} & r^{-(v_{k,n}+1)} \\ \sigma_{\mathrm{r},k}v_{k,n}r^{v_{k,n}-1} & -\sigma_{\mathrm{r},k}(v_{k,n}+1)r^{-(v_{k,n}+2)} \end{bmatrix}. \quad \text{(B5)}$$

Note that the transition matrices $\mathbf{C}_{k,n}$ are independent of the source's characteristics. The initial values for the recursion are

$$\begin{bmatrix} a_{0,1,n} \\ b_{0,1,n} \end{bmatrix} = \begin{bmatrix} 1 \\ 0 \end{bmatrix} \quad \text{(B6)}$$

and

$$\begin{bmatrix} a_{1,K,n} \\ b_{1,K,n} \end{bmatrix} = \begin{bmatrix} \dfrac{1+v_{K,n}}{v_{K,n}}r_K^{-(2v_{K,n}+1)} \\ 1 \end{bmatrix}. \quad \text{(B7)}$$

For completeness, the derivation of these equations can be found in Appendix C.

APPENDIX C: DERIVATION OF THE ELECTRIC POTENTIAL

In order to make the presentation self-contained and to help the reader to avoid the inconvenience of converting notations, this Appendix derives an expression for the electric potential inside a spherically symmetric conductor due to an internal quasi-static current dipole. The derivation follows that presented in Ref. 22, which is a generalization of the derivation of Ref. 19 allowing also the innermost layer to be anisotropic, using our notation and is here presented for an arbitrary source position and observation point. First, we will calculate the potential of a current monopole; the dipole potential is obtained from the monopole solution by differentiation.

Let us consider a current source s, which gives rise to current density $\boldsymbol{J}$ according to $\nabla\cdot\boldsymbol{J}(\boldsymbol{r}) = s(\boldsymbol{r})$, where $\boldsymbol{r}$ is the position. By writing $\boldsymbol{J}$ with the help of the conductivity $\boldsymbol{\sigma}$ and the electric potential V (see Sec. II A), we get

$$\nabla\cdot[\boldsymbol{\sigma}(\boldsymbol{r})\circ\nabla V(\boldsymbol{r})] = -s(\boldsymbol{r}) \quad \text{(C1)}$$

or, in spherical coordinates,

$$\frac{1}{r^2}\frac{\partial}{\partial r}\left[r^2\sigma_\mathrm{r}(r)\frac{\partial V}{\partial r}\right]+\frac{\sigma_\mathrm{t}(r)}{r^2\sin\theta}\frac{\partial}{\partial\theta}\left(\sin\theta\frac{\partial V}{\partial\theta}\right)+\frac{\sigma_\mathrm{t}(r)}{r^2\sin^2\theta}\frac{\partial^2 V}{\partial\phi^2}=-s(\boldsymbol{r}), \tag{C2}$$

where $\boldsymbol{\sigma}=[\sigma_\mathrm{r},\sigma_\mathrm{t},\sigma_\mathrm{t}]$.

For a monopolar current source $s(\boldsymbol{r})=I\delta(\boldsymbol{r}-\boldsymbol{r}_\mathrm{I})$ (strength I and location $\boldsymbol{r}_\mathrm{I}$), the solution of Eq. (C2) can be found using the separation of variables:

$$V_\mathrm{I}(\boldsymbol{r})=\sum_{n=0}^{\infty}R_n(r)\sum_{m=-n}^{n}Y_n^m(\theta_\mathrm{I},\phi_\mathrm{I})Y_n^m(\theta,\phi) \tag{C3}$$

where R_n is a function to be determined. Inserting V_I and the expression of s into Eq. (C2) leads to

$$\sum_{n=0}^{\infty}\sum_{m=-n}^{n}Y_n^m(\theta_\mathrm{I},\phi_\mathrm{I})Y_n^m(\theta,\phi)\frac{1}{r^2}\left\{\frac{\partial}{\partial r}\left[r^2\sigma_\mathrm{r}(r)\frac{\partial R_n(r)}{\partial r}\right]+-n(n+1)\sigma_\mathrm{t}(r)R_n(r)\right\}=-I\delta(\boldsymbol{r}-\boldsymbol{r}_\mathrm{I}) \tag{C4}$$

as the spherical harmonics are eigenfunctions of the angular part of Eq. (C2).[30] Multiplying Eq. (C4) by $Y_{n'}^{m'}(\theta,\phi)r^2\sin\theta$ and integrating it over θ and ϕ gives, with the help of Eq. (A2),

$$\frac{\partial}{\partial r}\left(r^2\sigma_\mathrm{r}(r)\frac{\partial R_n(r)}{\partial r}\right)-n(n+1)\sigma_\mathrm{t}(r)R_n(r)=-I\delta(r-r_\mathrm{I}). \tag{C5}$$

In order to solve Eq. (C5), we will restrict the analysis to a piecewise constant conductivity, which in the region between the surfaces $k-1$ and k of the layered spherical conductor is given by $\boldsymbol{\sigma}_k=[\sigma_{\mathrm{r},k},\sigma_{\mathrm{t},k},\sigma_{\mathrm{t},k}]$. In this case, the solution of Eq. (C5) within the kth layer can be written as

$$R_{k,n}(r)=\begin{cases}c_{0,k,n}\left(a_{0,k,n}r^{v_{k,n}}+b_{0,k,n}r^{-(v_{k,n}+1)}\right), & r\le r_\mathrm{I}\\ c_{1,k,n}\left(a_{1,k,n}r^{v_{k,n}}+b_{1,k,n}r^{-(v_{k,n}+1)}\right), & r_\mathrm{I}\le r,\end{cases} \tag{C6}$$

where

$$v_{k,n}=\sqrt{n(n+1)\sigma_{\mathrm{t},k}/\sigma_{\mathrm{r},k}+1/4}-1/2 \tag{C7}$$

and $a_{\xi,k,n}$, $b_{\xi,k,n}$, and $c_{\xi,k,n}$ are constants to be determined. Let k_I refer to the compartment containing the monopole source: $r_{k_\mathrm{I}-1}<r_\mathrm{I}<r_{k_\mathrm{I}}$. By requiring the continuity of the potential at $r=r_\mathrm{I}$ and by integrating Eq. (C5) over a region of infinitesimal length centered at r_I, we obtain two equations, which can be solved to yield

$$R_{k,n}(r)=c_n\begin{cases}(a_{0,k,n}r^{v_{k,n}}+b_{0,k,n}r^{-(v_{k,n}+1)})(a_{1,k,n}r_\mathrm{I}^{v_{k,n}}+b_{1,k,n}r_\mathrm{I}^{-(v_{k,n}+1)}), & r\le r_\mathrm{I}\\ (a_{0,k,n}r_\mathrm{I}^{v_{k,n}}+b_{0,k,n}r_\mathrm{I}^{-(v_{k,n}+1)})(a_{1,k,n}r^{v_{k,n}}+b_{1,k,n}r^{-(v_{k,n}+1)}), & r_\mathrm{I}\le r,\end{cases} \tag{C8}$$

where

$$c_n=\frac{I}{(2v_{k_\mathrm{I},n}+1)\sigma_{\mathrm{r},k_\mathrm{I}}(a_{0,k_\mathrm{I},n}b_{1,k_\mathrm{I},n}-a_{1,k_\mathrm{I},n}b_{0,k_\mathrm{I},n})}. \tag{C9}$$

The form of Eq. (C8) is valid in every compartment k (not only in k_I), as by varying $a_{\xi,k,n}$ and $b_{\xi,k,n}$ all values of $c_{\xi,k,n}$ can be achieved. To avoid unphysical divergence at the origin, we require $b_{0,1,n}=0$. We are also allowed to choose $a_{0,1,n}=1$, as it only multiplies $a_{1,1,n}$ and $b_{1,1,n}$.

The remaining coefficients $a_{\xi,k,n}$ and $b_{\xi,k,n}$ are found by requiring that the appropriate boundary conditions are satisfied: the electric potential and the normal component of the current density have to be continuous across the surfaces. This leads to the following relation between the coefficients:

$$\begin{bmatrix}a_{\xi,k+1,n}\\ b_{\xi,k+1,n}\end{bmatrix}=\mathbf{C}_{k+1,n}^{-1}(r_k)\mathbf{C}_{k,n}(r_k)\begin{bmatrix}a_{\xi,k,n}\\ b_{\xi,k,n}\end{bmatrix}, \tag{C10}$$

where

$$\mathbf{C}_{k,n}(r)=\begin{bmatrix}r^{v_{k,n}} & r^{-(v_{k,n}+1)}\\ \sigma_{\mathrm{r},k}v_{k,n}r^{v_{k,n}-1} & -\sigma_{\mathrm{r},k}(v_{k,n}+1)r^{-(v_{k,n}+2)}\end{bmatrix} \tag{C11}$$

is a source-independent transition matrix. The initial values

$$\begin{bmatrix}a_{0,1,n}\\ b_{0,1,n}\end{bmatrix}=\begin{bmatrix}1\\ 0\end{bmatrix} \tag{C12}$$

were justified earlier. Another set of initial values follows from the requirement that the current may not flow across the outer boundary of the sphere ($\partial V/\partial r|_{r_K}=0$, i.e., $\partial R_{K,n}/\partial r|_{r_K}=0$):

$$\begin{bmatrix}a_{1,K,n}\\ b_{1,K,n}\end{bmatrix}=\begin{bmatrix}\frac{1+v_{K,n}}{v_{K,n}}r_K^{-(2v_{K,n}+1)}\\ 1\end{bmatrix}. \tag{C13}$$

In principle, the boundary condition gives $a_{1,K,n}$ and $b_{1,K,n}$ only up to a common constant factor. However, the natural choice $b_{1,K,n}=1$ in Eq. (C13) follows from the fact that in Eq. (C8) this factor appears both in the numerator and denominator and thus has no effect on $R_{k,n}(r)$. As pointed out in Ref. 22, although Eq. (C9) formally depends on the source position, it turns out to be independent of r_I; thus, it is convenient to evaluate its value within the innermost layer:

$$c_n=\frac{I}{(2v_{1,n}+1)\sigma_{\mathrm{r},1}b_{1,1,n}}. \tag{C14}$$

Now, the monopole potential can be written as

$$V_{\mathrm{I}}(\boldsymbol{r}) = \sum_{n=0}^{\infty}\sum_{m=-n}^{n} I_n^m(\boldsymbol{r}_{\mathrm{I}})(a_{\xi,k,n} r^{v_{k,n}} + b_{\xi,k,n} r^{-(v_{k,n}+1)}) Y_n^m(\theta,\phi), \quad r_{k-1} \le r \le r_k, \tag{C15}$$

where

$$I_n^m(\boldsymbol{r}_{\mathrm{I}}) = \frac{I}{(2v_{1,n}+1)\sigma_{\mathrm{r},1} b_{1,1,n}} Y_n^m(\theta_{\mathrm{I}},\phi_{\mathrm{I}}) \times \left(a_{1-\xi,k_{\mathrm{I}},n} r_{\mathrm{I}}^{v_{k_{\mathrm{I}},n}} + b_{1-\xi,k_{\mathrm{I}},n} r_{\mathrm{I}}^{-(v_{k_{\mathrm{I}},n}+1)}\right) \tag{C16}$$

and ξ serves the purpose of separating the spherical volume into two regions allowing us to make the presentation more compact: when $r < r_{\mathrm{I}}$, $\xi = 0$, and when $r > r_{\mathrm{I}}$, $\xi = 1$.

The potential due to a current dipole is obtained with the help of Eq. (C15) by placing two current monopoles (amplitudes $\pm I$) at $\boldsymbol{r}_{\mathrm{Q}} - \boldsymbol{\delta}/2$ ($-I$) and at $\boldsymbol{r}_{\mathrm{Q}} + \boldsymbol{\delta}/2$ ($+I$), where $\boldsymbol{\delta}$ is their separation, and taking the limit $|\boldsymbol{\delta}| \to 0$. This procedure leads to the potential of a current dipole located at $\boldsymbol{r}_{\mathrm{Q}}$:

$$V(\boldsymbol{r}) = \lim_{|\boldsymbol{\delta}|\to 0} \boldsymbol{\delta}\cdot\nabla_{\boldsymbol{r}_{\mathrm{Q}}} V_{\mathrm{I}}(\boldsymbol{r},\boldsymbol{r}_{\mathrm{Q}}) = \boldsymbol{Q}\cdot\nabla_{\boldsymbol{r}_{\mathrm{Q}}} V_{\mathrm{I}}(\boldsymbol{r},\boldsymbol{r}_{\mathrm{Q}})/I, \tag{C17}$$

where the dipole moment $\boldsymbol{Q} = \boldsymbol{\delta} I$ and $\nabla_{\boldsymbol{r}_{\mathrm{Q}}}$ refers to differentiation with respect to the source coordinates. Thus, the last step in deriving the dipole potential is to calculate the coefficients

$$Q_n^m(\boldsymbol{r}_{\mathrm{Q}}) = \boldsymbol{Q}\cdot\nabla_{\boldsymbol{r}_{\mathrm{Q}}} I_n^m(\boldsymbol{r}_{\mathrm{Q}})/I. \tag{C18}$$

Taking advantage of the real vector spherical harmonics, Eqs. (A3) and (A5), allows us to transform Eq. (C18) into Eq. (B2) and to obtain Eq. (B1).

APPENDIX D: ASYMPTOTIC BEHAVIOR

In this Appendix, we analyze how the terms in the series of Eq. (14) behave when $n \gg 1$. First, we note that Eq. (B3) simplifies to $v_{k,n} \approx n\lambda_k$, where $\lambda_k = \sqrt{\sigma_{\mathrm{t},k}/\sigma_{\mathrm{r},k}}$. Then, Eq. (B2) becomes

$$Q_n^m(\boldsymbol{r}_{\mathrm{Q}}) \approx \frac{1}{\lambda_1}\frac{\boldsymbol{Q}}{\sqrt{2}\sigma_{\mathrm{r},1} b_{1,1,n} r_{\mathrm{Q}}^2 r_{\mathrm{Q}}^{v_{k_{\mathrm{Q}},n}}} \cdot \left[\lambda_{k_{\mathrm{Q}}}, 1, 1\right] \circ \left[a_{1-\xi,k_{\mathrm{Q}},n} r_{\mathrm{Q}}^{2v_{k_{\mathrm{Q}},n}+1} \boldsymbol{Y}_{n,n-1}^m(\theta_{\mathrm{Q}},\phi_{\mathrm{Q}}) + b_{1-\xi,k_{\mathrm{Q}},n} \boldsymbol{Y}_{n,n+1}^m(\theta_{\mathrm{Q}},\phi_{\mathrm{Q}})\right]. \tag{D1}$$

After simplification, Eqs. (B4)–(B7) can be written as follows:

$$a_{0,k,n} \approx \prod_{i=1}^{k-1} \frac{1}{2} r_i^{v_{i,n}-v_{i+1,n}} \left(1 + \frac{\lambda_i}{\lambda_{i+1}}\frac{\sigma_{\mathrm{r},i}}{\sigma_{\mathrm{r},i+1}}\right), \tag{D2}$$

$$b_{0,k,n} \approx r_{k-1}^{1+2v_{k,n}} \prod_{i=1}^{k-1} \frac{1}{2} r_i^{v_{i,n}-v_{i+1,n}} \left[1 + (-1)^{\delta_{i(k-1)}} \frac{\lambda_i}{\lambda_{i+1}}\frac{\sigma_{\mathrm{r},i}}{\sigma_{\mathrm{r},i+1}}\right], \tag{D3}$$

$$a_{1,k,n} \approx r_k^{-(1+2v_{k,n})} \prod_{i=k+1}^{K} \frac{1}{2} r_{i-1}^{v_{i-1,n}-v_{i,n}} \left[1 + (-1)^{\delta_{i(k+1)}} \frac{\lambda_i}{\lambda_{i-1}}\frac{\sigma_{\mathrm{r},i}}{\sigma_{\mathrm{r},i-1}}\right], \tag{D4}$$

$$b_{1,k,n} \approx \prod_{i=k+1}^{K} \frac{1}{2} r_{i-1}^{v_{i-1,n}-v_{i,n}} \left(1 + \frac{\lambda_i}{\lambda_{i-1}}\frac{\sigma_{\mathrm{r},i}}{\sigma_{\mathrm{r},i-1}}\right), \tag{D5}$$

where δ_{ij} is the Kronecker delta and $r_0 = 0$. When $n \gg 1$, the series terms in the toroidal component of the magnetic field, $\boldsymbol{B}^{\mathrm{t}} = \sum_{n=1}^{\infty}\sum_{m=-n}^{n} \boldsymbol{B}_n^{\mathrm{t},m}$, simplify to

$$\boldsymbol{B}_n^{\mathrm{t},m}(\boldsymbol{r}) \approx \mu_0 \sigma_{\mathrm{r},k}\lambda_k Q_n^m(\boldsymbol{r}_{\mathrm{Q}}) r^{v_{k,n}} (a_{\xi,k,n} - r^{-(2v_{k,n}+1)} b_{\xi,k,n}) \times \boldsymbol{Y}_{n,n}^m(\theta,\phi), \quad r_{k-1} \le r \le r_k, r \ne r_{\mathrm{Q}}. \tag{D6}$$

Finally, with the help of Eqs. (D2)–(D5), we write Eq. (D6) separately for $r < r_{\mathrm{Q}}$ ($\xi = 0$) and $r > r_{\mathrm{Q}}$ ($\xi = 1$)

$$\boldsymbol{B}_n^{\mathrm{t},m}(\boldsymbol{r}) \approx \frac{\mu_0\lambda_k\sigma_{\mathrm{r},k} b_{1,k_{\mathrm{Q}},n} a_{0,k,n}}{\sqrt{2}\lambda_1\sigma_{\mathrm{r},1} b_{1,1,n} r_{\mathrm{Q}}^2} \frac{r^{v_{k,n}}}{r_{\mathrm{Q}}^{v_{k_{\mathrm{Q}},n}}} \boldsymbol{Q} \cdot \left\{\left[\lambda_{k_{\mathrm{Q}}}, 1, 1\right] \circ \boldsymbol{Y}_{n,n+1}^m(\theta_{\mathrm{Q}},\phi_{\mathrm{Q}})\right\} \boldsymbol{Y}_{n,n}^m(\theta,\phi), \quad r_{k-1} \le r \le r_k, r < r_{\mathrm{Q}}, \tag{D7}$$

$$\boldsymbol{B}_n^{\mathrm{t},m}(\boldsymbol{r}) \approx -\frac{\mu_0\lambda_k\sigma_{\mathrm{r},k} b_{1,k,n} a_{0,k_{\mathrm{Q}},n}}{\sqrt{2}\lambda_1\sigma_{\mathrm{r},1} b_{1,1,n} r_{\mathrm{Q}}^2} \frac{r_{\mathrm{Q}}^{v_{k_{\mathrm{Q}},n}+1}}{r^{v_{k,n}+1}} \boldsymbol{Q} \cdot \left\{\left[\lambda_{k_{\mathrm{Q}}}, 1, 1\right] \circ \boldsymbol{Y}_{n,n-1}^m(\theta_{\mathrm{Q}},\phi_{\mathrm{Q}})\right\} \boldsymbol{Y}_{n,n}^m(\theta,\phi), \quad r_{k-1} \le r \le r_k, r > r_{\mathrm{Q}}. \tag{D8}$$

Equations (D7) and (D8) show that for large n and isotropic conductivity the series terms scale as $(r/r_{\mathrm{Q}})^n$ and $(r_{\mathrm{Q}}/r)^{n+1}$, when $r < r_{\mathrm{Q}}$ and $r > r_{\mathrm{Q}}$, respectively.

APPENDIX E: HOMOGENEOUS ISOTROPIC SPHERE

The magnetic field inside a homogeneous isotropic sphere due to an internal quasi-static current dipole has a closed-form solution[17]

$$\boldsymbol{B}_{\mathrm{homog}}^{\mathrm{cf}}(\boldsymbol{r}) = \frac{\mu_0}{4\pi}\left[\boldsymbol{Q}\times\left(\frac{\boldsymbol{\alpha}}{\alpha^3} - \frac{r}{r_K}\frac{\boldsymbol{\beta}}{\beta^3}\right) + \left(\frac{r}{r_K}\right)^3 \times \frac{1}{H^2}(H\boldsymbol{Q}\times\boldsymbol{r}_{\mathrm{Q}} - \boldsymbol{Q}\times\boldsymbol{r}_{\mathrm{Q}}\cdot\boldsymbol{r}\boldsymbol{K})\right], \quad r < r_K, \tag{E1}$$

where r_K is the radius of the sphere, $\boldsymbol{\alpha} = \boldsymbol{r} - \boldsymbol{r}_{\mathrm{Q}}$, $\boldsymbol{\beta} = (r_K/r)\boldsymbol{r} - (r/r_K)\boldsymbol{r}_{\mathrm{Q}}$, $H = \beta(\boldsymbol{r}\cdot\boldsymbol{\beta} + r\beta)$, and

$$\boldsymbol{K} = \left(\frac{r_K}{r}\frac{H}{\beta^2} + \beta + r_K\right)\boldsymbol{\beta} + \left(\frac{r_K}{r}\beta + \frac{\beta^2}{r}\right)\boldsymbol{r}. \tag{E2}$$

[1] M. Hämäläinen, R. Hari, R. J. Ilmoniemi, J. Knuutila, and O. V. Lounasmaa, Rev. Mod. Phys. **65**, 413 (1993).
[2] J. Bodurka, A. Jesmanowicz, J. S. Hyde, H. Xu, L. Estkowski, and S.-J. Li, J. Magn. Reson. **137**, 265 (1999).
[3] J. Bodurka and P. A. Bandettini, Magn. Reson. Med. **47**, 1052 (2002).
[4] N. Petridou, D. Plenz, A. C. Silva, M. Loew, J. Bodurka, and P. A. Bandettini, Proc. Natl. Acad. Sci. U.S.A. **103**, 16015 (2006).
[5] R. H. Kraus, Jr., P. Volegov, A. Matlachov, and M. Espy, Neuroimage **39**, 310 (2008).
[6] M. Burghoff, H. H. Albrecht, S. Hartwig, I. Hilschenz, R. Körber, N. Höfner, H.-J. Scheer, J. Voigt, L. Trahms, and G. Curio, Appl. Phys. Lett. **96**, 233701 (2010).

[7]R. Körber, J. O. Nieminen, N. Höfner, V. Jazbinsek, H.-J. Scheer, K. Kim, and M. Burghoff, J. Magn. Reson. **237**, 182 (2013).
[8]J. R. Maze, P. L. Stanwix, J. S. Hodges, S. Hong, J. M. Taylor, P. Cappellaro, L. Jiang, M. V. G. Dutt, E. Togan, A. S. Zibrov, A. Yacoby, R. L. Walsworth, and M. D. Lukin, Nature **455**, 644 (2008).
[9]J. M. Taylor, P. Cappellaro, L. Childress, L. Jiang, D. Budker, P. R. hemmer, A. Yacoby, R. Walsworth, and M. D. Lukin, Nat. Phys. **4**, 810 (2008).
[10]A. Cooper, E. Magesan, H. N. Yum, and P. Cappellaro, Nat. Commun. **5**, 3141 (2014).
[11]L. Caruso, E. Paul, A. Demonti, C. Fermon, M. Pannetier-Lecoeur, G. Ouanounou, A. Mikroulis, and T. Bal, "Mapping the electromagnetic field of neurons at cellular scale using ultra-sensitive magnetometer," in *Proceedings of the 19th International Conference on Biomagnetism*, Halifax, NS, Canada, Aug. 24–28 (2014).
[12]M. Stenroos, A. Hunold, and J. Haueisen, Neuroimage **94**, 337 (2014).
[13]C. H. Wolters, A. Anwander, X. Tricoche, D. Weinstein, M. A. Koch, and R. S. MacLeod, Neuroimage **30**, 813 (2006).
[14]J. Sarvas, Phys. Med. Biol. **32**, 11 (1987).
[15]R. J. Ilmoniemi, Europhys. Lett. **30**, 313 (1995).
[16]S. He, IEEE Trans. Biomed. Eng. **45**, 1249 (1998).
[17]L. Heller, D. Ranken, and E. Best, IEEE Trans. Biomed. Eng. **51**, 1310 (2004).
[18]R. S. Hosek, A. Sances, Jr., R. W. Jodat, and S. J. Larson, IEEE Trans. Biomed. Eng. **25**, 405 (1978).
[19]J. C. de Munck, J. Appl. Phys. **64**, 464 (1988).
[20]J. C. de Munck and M. J. Peters, IEEE Trans. Biomed. Eng. **40**, 1166 (1993).
[21]J. C.-E. Sten, IEEE Trans. Dielectr. Electr. Insul. **2**, 360 (1995).
[22]Y. Petrov, Phys. Rev. E **86**, 011917 (2012).
[23]Elekta Neuromag, *Elekta Neuromag® System Hardware User's Manual*, 7th ed. (Elekta Neuromag Oy, 2005).
[24]J. O. Nieminen, L. M. Koponen, and R. J. Ilmoniemi, Brain Stimul. **8**, 582 (2015).
[25]A. Crouzeix, B. Yvert, O. Bertrand, and J. Pernier, Clin. Neurophysiol. **110**, 2176 (1999).
[26]G. Marin, C. Guerin, S. Baillet, L. Garnero, and G. Meunier, Hum. Brain Mapp. **6**, 250 (1998).
[27]S. Lew, C. H. Wolters, T. Dierkes, C. Röer, and R. S. MacLeod, Appl. Numer. Math. **59**, 1970 (2009).
[28]M. Stenroos and J. Sarvas, Phys. Med. Biol. **57**, 3517 (2012).
[29]R. Plonsey and D. B. Heppner, B. Math. Biophys. **29**, 657 (1967).
[30]J. D. Jackson, *Classical Electrodynamics*, 3rd ed. (Wiley, 1999).
[31]A. Prosperetti, *Advanced Mathematics for Applications* (Cambridge University Press, New York, USA, 2011).
[32]D. B. Geselowitz, IEEE Trans. Magn. **6**, 346 (1970).
[33]M. J. Peters and P. J. H. Elias, Med. Biol. Eng. Comput. **26**, 617 (1988).
[34]H. Zhou and A. van Oosterom, IEEE Trans. Biomed. Eng. **39**, 154 (1992).
[35]S. B. Baumann, D. R. Wozny, S. K. Kelly, and F. M. Meno, IEEE Trans. Biomed. Eng. **44**, 220 (1997).
[36]A. Pfefferbaum, E. V. Sullivan, M. Hedehus, K. O. Lim, E. Adalsteinsson, and M. Moseley, Magn. Reson. Med. **44**, 259 (2000).
[37]D. H. Salat, D. S. Tuch, D. N. Greve, A. J. W. van der Kouwe, N. D. Hevelone, A. K. Zaleta, B. R. Rosen, B. Fischl, S. Corkin, H. D. Rosas, and A. M. Dale, Neurobiol. Aging **26**, 1215 (2005).
[38]M. Dannhauer, B. Lanfer, C. H. Wolters, and T. R. Knösche, Hum. Brain Mapp. **32**, 1383 (2010).
[39]H. Buchner, G. Knoll, M. Fuchs, A. Rienäcker, R. Beckmann, M. Wagner, J. Silny, and J. Pesch, Electroencephalogr. Clin. Neurophysiol. **102**, 267 (1997).
[40]T. Medani, D. Lautru, D. Schwartz, Z. Ren, and G. Sou, Prog. Electromagn. Res. **153**, 11 (2015).
[41]D. E. Winch, D. J. Ivers, J. P. R. Turner, and R. J. Stening, Geophys. J. Int. **160**, 487 (2005).
[42]E. T. Whittaker and G. N. Watson, *A Course of Modern Analysis*, 4th ed. (Cambridge University Press, New York, USA, 1927).
[43]J. M. Blatt and V. F. Weisskopf, *Theoretical Nuclear Physics* (Springer-Verlag, New York, 1952), Appendix B.
[44]E. L. Hill, Am. J. Phys. **22**, 211 (1954).
[45]S. K. Stanaway, B. J. Cantwell, and P. R. Spalart, "A numerical study of viscous vortex rings using a spectral method," Technical Memorandum 101041 (NASA, 1988), Appendix B.